

Atlas-Based Automatic Generation of Subject-Specific Finite Element Tongue Meshes

AHMAD BIJAR,^{1,2,4,5} PIERRE-YVES ROHAN,³ PASCAL PERRIER,^{4,5} and YOHAN PAYAN^{1,2}

¹Univ. Grenoble Alpes, TIMC-IMAG, 38000 Grenoble, France; ²CNRS, TIMC-IMAG, 38000 Grenoble, France; ³LBM/ Institut de Biomécanique Humaine Georges Charpak, 151 Boulevard de l'Hôpital, 75013 Paris, France; ⁴Univ. Grenoble Alpes, Gipsa-lab, 38000 Grenoble, France; and ⁵CNRS, Gipsa-lab, 38000 Grenoble, France

(Received 16 April 2015; accepted 27 October 2015; published online 17 November 2015)

Associate Editor Karol Miller oversaw the review of this article.

Abstract—Generation of subject-specific 3D finite element (FE) models requires the processing of numerous medical images in order to precisely extract geometrical information about subject-specific anatomy. This processing remains extremely challenging. To overcome this difficulty, we present an automatic atlas-based method that generates subject-specific FE meshes *via* a 3D registration guided by Magnetic Resonance images. The method extracts a 3D transformation by registering the atlas' volume image to the subject's one, and establishes a one-to-one correspondence between the two volumes. The 3D transformation field deforms the atlas' mesh to generate the subject-specific FE mesh. To preserve the quality of the subject-specific mesh, a diffeomorphic non-rigid registration based on B-spline free-form deformations is used, which guarantees a non-folding and one-to-one transformation. Two evaluations of the method are provided. First, a publicly available CT-database is used to assess the capability to accurately capture the complexity of each subject-specific Lung's geometry. Second, FE tongue meshes are generated for two healthy volunteers and two patients suffering from tongue cancer using MR images. It is shown that the method generates an appropriate representation of the subject-specific geometry while preserving the quality of the FE meshes for subsequent FE analysis. To demonstrate the importance of our method in a clinical context, a subject-specific mesh is used to simulate tongue's biomechanical response to the activation of an important tongue muscle, before and after cancer surgery.

Keywords—Tongue model, Patient-specific, Finite element model, Mesh morphing, Volume image registration, Biomechanical simulation.

Address correspondence to Ahmad Bijar, Univ. Grenoble Alpes, TIMC-IMAG, 38000 Grenoble, France. Electronic mails: ahmad.bijar@imag.fr, pierre-yves.rohan@ensam.eu, Pascal.Perrier@gipsa-lab.grenoble-inp.fr and yohan.payan@imag.fr

INTRODUCTION

FE models are used extensively in computer-aided surgery. For such contexts subject-specific models need to be generated. However, the generation of each mesh requires the processing of numerous medical images in order to precisely extract geometrical information about subject-specific anatomy. This can be extremely time consuming because it involves segmentation and meshing processes. In the literature a wide range of scenarios is reported under different levels of automation, in order to refine the results by improving segmentation, surface creation and/or meshing processes. The primary purpose of all these studies is to make FE mesh generation compatible with the time constraints of the clinical practice where the pre/intra-operative time-window is short and clinician availability is limited. Below a brief overview of these efforts is provided and our contribution to this problem is described.

Two main strategies exist to improve volumetric mesh generation algorithms: Meshing-based procedures, and Atlas-based mesh morphing techniques. A large variety of methods published in the literature and of commercial software products are classified among the Meshing-based procedures; most of them use tetrahedral meshing algorithms.^{48,63} 3D surface models, usually obtained with segmentation techniques, are inputs for these methods and some post-processing techniques (e.g., smoothing, cleanup and refinement) might be necessary. Some of these methods generate 3D FE meshes including anatomical sub-structures inside.^{19,37,47,66,67} Mention should also be made of the numerical locking issues that may occur in FE analysis

of incompressible or nearly-incompressible materials (e.g., soft tissues).⁵⁴ Hexahedral FE meshes are preferred to tetrahedral ones⁷ for this kind of materials. However, automatic hexahedral mesh generation,^{32,62} is a challenging research topic.^{58,61} Current hexahedral meshing algorithms commonly require user intervention and are labor intensive.⁴⁶ An alternative to all-tetrahedral and all-hexahedral element meshes is to use mixed-element meshing. The overall idea is to take advantage of the benefits of both element types. We recently reported a new automatic meshing technique.⁴¹ This algorithm was used to generate the atlas' tongue mesh.

Atlas-based mesh morphing techniques show a great potential for subject-specific FE mesh generation and are increasingly employed.^{12,15,20,27,57} These methods first need an atlas' FE mesh, which can be designed following usual procedures. The subsequent step is the extraction of information related to specific region of interest (ROI) from subject's medical images. It can be extracted in the form of contours, 3D surface models, or a set of land-marks. Finally, the atlas' FE mesh is "morphed" onto the ROI's information and subject-specific meshes are automatically generated.

Alternatively, with the aim of avoiding extraction of formal geometrical description in the ROIs, which can be complicated, some methods register either an atlas' binary mask previously generated from the atlas' mesh, or idealized synthetic images of the atlas onto the subject's images. These methods extract a 3D displacement field that can be used to morph the atlas' FE mesh.^{6,35,36} The main advantage of these techniques is that all the meshes inherit the same structure from the atlas' FE mesh (same nodes and same elements' organization). It should be noted that after morphing the quality of the meshes may decrease, and post-processing refinement procedures are often required.¹³ The level of distortion is also depending on the complexity of the atlas' and subject's geometries. Some researchers have employed meshing-based procedures and atlas-based FE mesh morphing techniques simultaneously.³⁰

Regardless of these improvements, most of these methods need extraction of some prior-knowledge about the organ's geometry from subjects' medical images. This is a challenging task, which can be time-consuming, especially for some applications requiring segmentation. In some cases the segmentation procedure is sensitive to noise or image quality. In such cases there is a need for methods that avoid the segmentation step. An atlas-based mesh morphing techniques offer an interesting alternative, if the 3D transformation that morphs the atlas' mesh into the subject's mesh can be inferred without any segmentation. Our objective is to propose a method that enables auto-

matic generation of subject-specific FE meshes by intensity-based image registration.

Our team has been working on the generation of subject-specific FE meshes over a long period of time. As compared to usual strategies the primary improvement was achieved by introducing the Mesh-Matching algorithm.¹⁵ However, the generated meshes were prone to distortions (see Refs. 12,13,27,30 for more details). Hence, the Mesh-Matching method was improved into the Mesh-Match-and-Repair (MMRep) algorithm¹² (Fig. 1). A ROI is segmented in the subject's images and its 3D surface is used as the target to deform the atlas' FE mesh. It was shown that the level of distortion can be dramatically reduced, if the transformation satisfies three main constraints: being C^1 -differentiable, non-folding (a local property ensuring that space orientation is preserved) and invertible; these properties specify a C^1 -diffeomorphism.^{12,14}

Our method (Fig. 2) takes inspiration from these pioneer works. In particular, it has to be a C^1 -diffeomorphism, in order to avoid unacceptable spatial distortions. It includes two major modules:

- Computing without any segmentation the displacement fields that can be used to register the volumetric atlas' images onto the subject's images;
- Morphing the atlas' FE mesh using the obtained displacement fields.

More specifically, at first, an initial Rigid/Affine transformation is performed to roughly approximate the global deformation between the atlas' and the subject's volume. Then, a non-rigid registration is done to locally refine the deformations from the atlas to the subject. The subject-specific FE mesh is then generated by deforming the atlas' FE mesh using the derived 3D transformation. Finally, the qualities of the morphed meshes are evaluated.

In the next sections, details of the method are provided and evaluated, and an illustration of its practical usability in a clinical context is proposed with an application in maxillo-facial computer-assisted intervention that requires the generation of patient-specific tongue FE meshes. This includes the volumetric image registration and the morphing of the atlas FE mesh. We propose as a first step an evaluation of our method based on a dataset of CT scans of the ribcage (including binary Lung masks) and consisting in evaluating the accuracy of the inter-subject registration process. In a second part tongue meshes are generated for two healthy subjects and two patients suffering from tongue cancer, with a particular focus on the assessment of the mesh's quality. Being able to generate accurate patient-specific tongue meshes is interest-

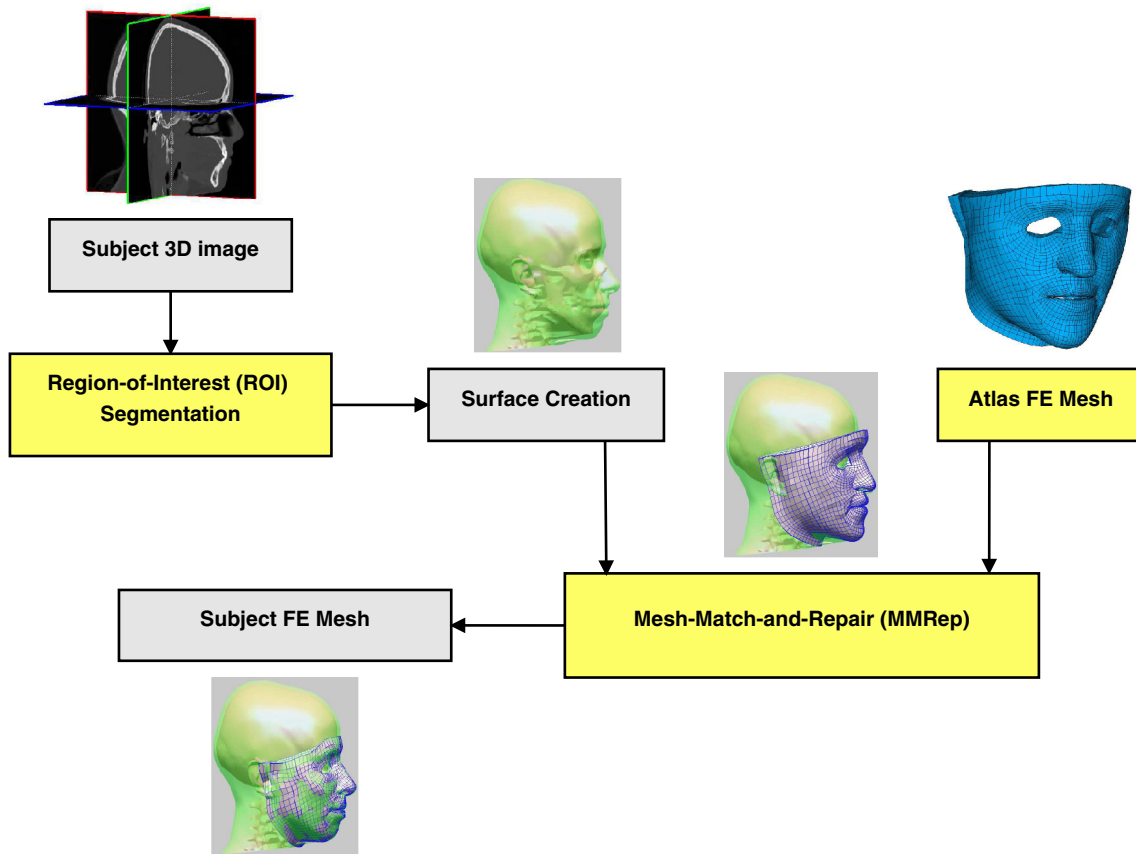


FIGURE 1. Block diagram of the Mesh-Match-and-Repair (MMRep) algorithm for generation of the 3D subject-specific FE meshes.¹²

ing because tongue segmentation from medical images is challenging²⁹ since the tongue is an extremely flexible organ that is in contact with many other structures in the oral cavity (cheeks, pharyngeal walls, palate, lips). Furthermore, regarding patients with abnormal structures (in the case of tongue cancers for example), as there will be intensity variations in the affected regions, automatic segmentation could be even more complex.^{28,38} Finally, the tongue model of one of the patients is used to qualitatively evaluate functional consequences of the surgery. The removal of the tumor and the replacement of the corresponding tissues with a passive flap are modeled. A tongue gesture is then simulated and analyzed, before and after surgery.

MATERIALS AND METHODS

Medical Images and FE Meshes

CT Scans of the Ribcage

EMPIRE10 competition, as part of MICCAI 2010 Grand Challenges, has provided 30 pairs of thoracic CT data.⁴⁹ CT scans are obtained for both healthy and

diseased subjects from various scanners with a variety of slice-spacings and image qualities. Most of the scans have a fine sub-millimeter image resolution (around 0.7 mm isotropic). The data include binary Lung masks which were generated automatically⁵⁹ and corrected manually when necessary. We considered the first fifteen subjects to evaluate the performance of our method. Considering the quality and resolution of the scans, volume #2 of the EMPIRE10 database was chosen to be the atlas.

Tongue MR Images and Atlas' FE Mesh

Our method was also employed to generate subject-specific FE tongue meshes. Tongue T1- or T2- weighted MR images of two healthy volunteers (S1 and S2) and two patients suffering from tongue cancer (P1 and P2) were obtained with a Philips 3T scanner system (respective repetition time/echo time: 426\10.74 ms, 3195.58\80 ms, 2000\29.27 ms, 400\10 ms). The image volume consisted of 32 sagittal slices with a 256×256 scan matrix and voxel dimensions of $1 \times 1 \times 5$ mm for S1, 72 sagittal slices with a 512×512 scan matrix and voxel dimensions of $0.45 \times 0.45 \times 2$ mm for S2,

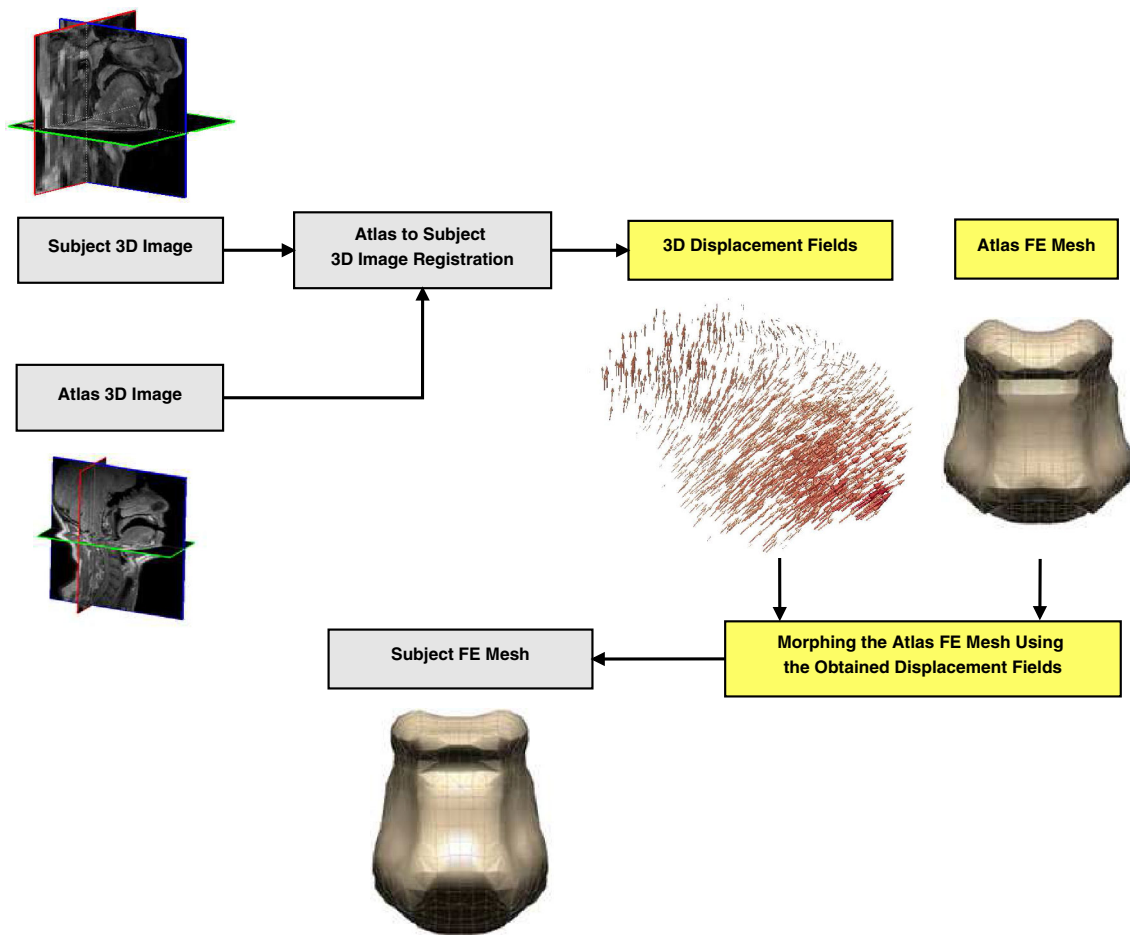


FIGURE 2. General dataflow proposed to generate 3D subject-specific FE meshes.

160 axial slices with a 224×224 scan matrix and voxel dimensions of $1 \times 1 \times 1$ mm for P1, and 29 sagittal slices with a 512×512 scan matrix and voxel dimensions of $0.5 \times 0.5 \times 3$ mm for P2. All subjects gave informed consent and the study had received approval from ethical committee of Grenoble University Hospital.

An atlas FE tongue mesh, which was previously elaborated in our group,¹¹ has been employed to generate subject-specific tongue FE meshes. The atlas' mesh was designed on the basis of 3D MR images of the vocal tract of a male subject, collected and segmented in the context of another study aiming at investigating the organization of articulatory configurations in the vocal tract during speech production.³ After building a surface mesh from the segmented images, the hex-dominant FE tongue mesh was automatically generated using a method that optimizes the process in terms of element quantity and quality.^{24,41,42,54} To assess the coarseness of the mesh, a mesh sensitivity analysis was performed based on the influence of the mesh density on the biomechanical

response of the tongue to the posterior genioglossus muscle activation (computed as the global displacement). The atlas' mesh is made of 2180 nodes forming 3172 elements: 796 tetrahedra, 766 pyramids, 432 wedges, and 1178 hexahedra. Figure 3 shows the atlas' MR images (25 sagittal slices with a 256×256 scan matrix and voxel dimensions of $1 \times 1 \times 4$ mm) superimposed to the tongue FE mesh.

Volume Image Registration

A two-level 3D image registration is used. First, a global transformation is calculated to provide an initial Rigid/Affine alignment. Then, a nonrigid method is used to establish the voxel-wise correspondence between the two volumes.

Two popular non-rigid diffeomorphic registration methods were proposed in the literature: (1) free-form deformations (FFDs), which are modeled by B-splines,⁵⁵ and (2) the diffeomorphic Demons, which is a nonparametric method based on Thirion's Demons algorithm.⁶⁰ FFDs-based registration algorithms are

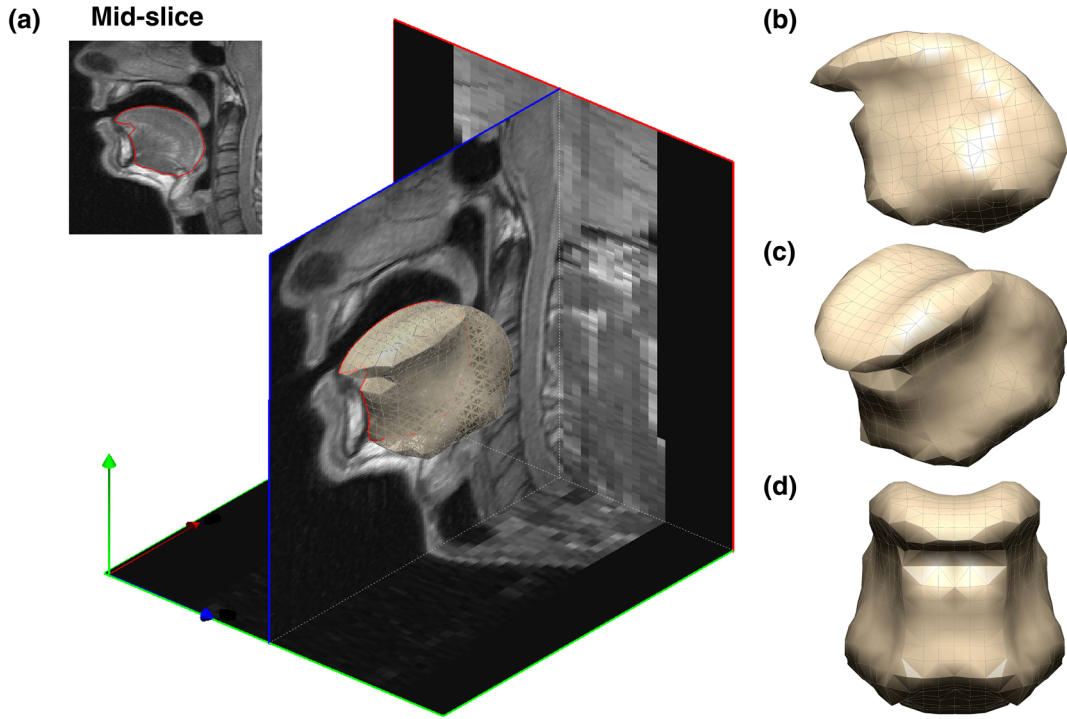


FIGURE 3. (a) Atlas' MR data superimposed with the 3D atlas' FE tongue mesh, (b) Side view, (c) isometric view and (d) front view respectively of the 3D FE tongue mesh.

controlled by the underlying interpolation function, which provides more regular displacement fields than Demons-based approaches. Our method uses the same FFDs-based method as.¹² In addition, the model is reformulated using discrete Markov random fields (MRF) (see below for details).^{26,34} In the next sections, the explanations of the diffeomorphic FFDs, their implementation and the employed optimization method are explained.

Free-Form Deformations

Non-rigid registration algorithms based on FFDs map each voxel of the atlas' image into the corresponding voxel in the subject' image using a deformation field that is optimally computed. The basic idea is to characterize deformations based on a grid of control points that are uniformly distributed throughout the fixed image's voxel grid (herein the subject's image). These control points partition the volume into equally sized regions (called *tiles*). The transformation model is a multilevel formulation of a FFD based on tensor product of B-splines. B-splines enable interpolating the dense deformation field from a given set of control points. Let us denote the domain of the image volume as $\Omega = \{(x, y, z) | 0 \leq x < X, 0 \leq y < Y, 0 \leq z < Z\}$. Let G denote a virtual deformable grid with spacings $\delta_x, \delta_y, \delta_z$, which is superimposed on the

image volume. The nonlinear displacement field D is computed for each image point $\mathbf{x} = (x, y, z)$ by B-spline interpolation of the displacements of the grid control points:

$$D(\mathbf{x}) = \sum_{l=0}^3 \sum_{m=0}^3 \sum_{n=0}^3 B_l(u)B_m(v)B_n(w)d_{i+l,j+m,k+n}, \quad (1)$$

where i, j , and k denote the coordinates of the *tile* containing \mathbf{x} , and u, v , and w are the local coordinates of (x, y, z) within its housing *tile*: $i = \lfloor x/\delta_x \rfloor, j = \lfloor y/\delta_y \rfloor, k = \lfloor z/\delta_z \rfloor, u = x/\delta_x - \lfloor x/\delta_x \rfloor, v = y/\delta_y - \lfloor y/\delta_y \rfloor, w = z/\delta_z - \lfloor z/\delta_z \rfloor$ ($\lfloor \cdot \rfloor$ means rounding). B_l and d respectively represent the l^{th} basis function of the B-spline interpolation and the displacement of the grid control points. Thus, $d_{i+l,j+m,k+n}$ is the spline coefficient defining the displacement for one of the 64 control points that influence the image point \mathbf{x} within *tile* (i, j, k) . Indeed, the B-splines serve as a weighted averaging function for the set of control points. Finally, the transformation of \mathbf{x} can be computed by

$$T(\mathbf{x}) = \mathbf{x} + D(\mathbf{x}) \quad (2)$$

Given the source (J) and target (I) volumes, one seeks the optimal transformation by posing an energy minimization problem where the objective function is defined by a matching criterion S :

$$\hat{T} = \arg \min_T S(I, J \circ T) \quad (3)$$

Depending on the application S may be either sum of absolute/squared differences (SAD/SSD), normalized mutual information,⁴³ normalized correlation coefficient, correlation ratio,⁵³ or any other user-defined function.

The performance of registration methods based on FFDs is limited by the resolution of the control point grid, which generally determines the degrees of freedom of the registration function and is linearly related to the computational complexity:⁵⁵

- A coarse control point spacing enables modeling global and intrinsically smooth deformations.
- A finer control point spacing enables modeling more localized and intrinsically less smooth deformations.

To refine the deformation field, a multi-level FFD is used, which covers a wide range of transformations. The algorithm starts from a coarser control point spacing; when the algorithm reaches its optimal state, the control point spacing is divided by two (in each dimension). For each level of control point spacing, several optimization cycles are performed to model a large deformation. Within each cycle, an elementary transformation field is generated and the overall transformation can be computed as:

$$T(\mathbf{x}) = \overbrace{T_j^{N_j} \circ \dots \circ T_j^1}^{G_j} \circ \dots \circ \overbrace{T_1^{N_1} \circ \dots \circ T_1^1}^{G_1}, \quad (4)$$

where $G_j, j = 1, \dots, J$ are successive grid refinements, and $T_j^i, i = 1, \dots, N_j$ are elementary deformations generated during each optimization cycle at grid level j . The initial control point spacing in the FFDs should be determined according to the application. As investigated in Ref. 26 when there is a good global correspondence between the volumes (provided by Rigid/Affine registration), employing an initial spacing of 20 mm enables capturing the key-features of the geometric structures accurately.²⁶ However, in case of organs with large anatomical differences such as the lungs or the feet, starting with a coarser control point spacing could be more efficient, since it enables the first level of the FFDs to include a reliable account of the Rigid/Affine transformation, providing thus a good initialization for the subsequent levels of the FFDs.

As the FFDs are modeled by B-splines, the transformation model inherently satisfies the C^1 -differentiability. In order to preserve the bijectivity of the transformation, each elementary transformation is estimated by restricting the displacement of control

points to 0.4 times the current control point spacing.⁵⁵ Since the overall transformation is computed as a combination of the elementary ones, it will be likewise a diffeomorphism. However, when the multilevel-FFD reaches its final levels, in which the control point grid has a high spatial resolution, the FFD models much more localized deformations; and it is likely that the distance between the neighboring nodes in the atlas FE mesh is much larger than the control point spacing. So, it is worth pointing out that although the restriction of displacements provides a non-folding property locally at every point, it certainly does not lead to regular meshes, especially in case of FE meshes with large elements. Therefore, an additional regularization term is considered:

$$R(T) = \sum_{p \in G} \sum_{q \in N(p)} |d_p - d_q|^2, \quad (5)$$

where d_p is the displacement of the control point p in the virtual deformable grid G , and $N(p)$ is the set of control points located in the neighborhood of p , and defines the edges between p and other points in the control grid. This regularization term, leads neighboring control points to move in the same direction. Hence, the total cost function includes two terms: a matching criterion (S) which quantifies the level of alignment between the two image volumes, and a regularization term (R) which imposes a smoothness constraint. The optimal transformation is determined by posing an energy minimization problem where the objective function is a weighted sum of S and R :

$$\hat{T} = \arg \min_T \{S(I, J \circ T) + \lambda R(T)\}, \quad (6)$$

where λ is a weighting factor controlling the influence of the regularization term. To obtain deformation parameters, a wide range of optimization strategies can be employed, including gradient descent,⁵⁶ Newton's method,^{45,64} Powell's method,⁵² and discrete optimization.⁵¹ Since the atlas' and subject's medical images can come from different modalities (e.g., CT or MRI), various similarity measures might be considered. In order to avoid problems associated with the computation of the derivatives of the Similarity Measure to be optimized, we implemented a discrete optimization method, namely a MRF-based optimization.³⁴

MRF-Based Optimization

An MRF-based optimization projects the objective function back to the level of the control points, in order to transform it into a function of control points displacements instead of voxels displacements. Then, the displacement space is sampled and the quantized

displacement vectors are associated with labels. Thus, the optimization problem is converted to a “labeling problem”. Finally, the optimization technique^{26,34} selects a group of displacement vectors that collectively optimize the objective function.

The primary task is the reformulation of the optimization problem (Eq. 6) into a multi-labeling problem that can be expressed using first-order MRFs.^{23,39} Generally a “labeling problem” consists of a set of objects to be classified and a set of classes or labels. The objective of such a problem is to assign a label to each object, in a way that is consistent with some observed data that may contain pairwise relationships among the objects to be classified.^{9,17,39} MRFs are used to model the statistical properties in the framework of the probability theory. In the MRFs model, the probability of an object to belong to a specific class depends not only on its own features but also on the labels of its neighboring objects. These objects are considered as random variables whose values result from probabilistic experiments. In MRFs, the set of labels is interpreted as events that can happen to the random variables.³⁹ Considering the registration problem, a random variable is associated with every control point, and “labels” correspond to the displacements of the control points. The continuous displacement space of the control points is quantized to generate a discrete set of displacement vectors $\Theta = \{d^1, \dots, d^i\}$, and each displacement vector is associated with a label ($L = \{l^1, \dots, l^i\}$). Assigning a label (l_p) to a control point (p) is equivalent to applying the displacement vector d^p to the control point p . The displacements along the coordinate axes are sparsely sampled by a factor of n , from 0 to 0.4 times the current control point spacing.⁵⁵ Thus $6n + 1$ labels (displacements along the six main axes plus the zero-displacement vector) are considered. The problem can be reformulated using the energy of first-order MRFs, which consists of sums of *unary* and *pairwise* potential functions:

$$E_{MRF}(l) = \sum_{p \in G} V_p(l_p) + \lambda \sum_{p \in G} \sum_{q \in N(p)} V_{pq}(l_p, l_q), \quad (7)$$

where l is the labeling that we are looking for, $V_p(\cdot)$ is a *unary* potential function that corresponds to the energy of assigning a label to the control point p , independently of all other control points.³⁹ The *unary* potential term summed over all the control points encodes the matching criterion (S) in Eq. (6). $V_{pq}(\cdot)$ is a *pairwise* potential function that evaluates the consistency between the labels of neighboring control points. It measures the cost of assigning displacements to the neighboring control points p and q . Therefore, the *pairwise* potential term summed over all the neighboring control points corresponds to the regularization term (R) in Eq. (6). It is important to note that the

matching criterion (S) is defined at the image level. This criterion must therefore be projected back to the control points level using a weighting function so that the energy optimization problem could be mathematically reformulated using MRFs:

$$\widehat{\eta}(|\mathbf{x} - p|) = \frac{\eta(|\mathbf{x} - p|)}{\sum_{y \in \Omega} \eta(|\mathbf{y} - p|)}, \quad (8)$$

where $\widehat{\eta}(\cdot)$ quantifies the impact of an image pixel \mathbf{x} to a control point p , while $\eta(\cdot)$, quantifies the influence of a control point p to an image pixel \mathbf{x} . The amount of influence is related to the distance between the image pixel \mathbf{x} and the control point p ; the farther they are, the less is the influence, and vice versa. Herein, the $\eta(\cdot)$ function is the B-spline function used in Eq. (1), that can be interpreted as a weighting function. Therefore, the *unary* potential function in the energy of MRF (in iteration t) can be rewritten as:

$$V_p(l_p) = \sum_{\mathbf{x} \in \Omega} \widehat{\eta}(|\mathbf{x} - p|) \cdot S(I(\mathbf{x}), J(T^{t-1}(\mathbf{x}) + d^p)), \quad (9)$$

where T^{t-1} is the overall transformation from the previous iteration and d^p is the next elementary displacement of control point p . Accordingly, the *unary* potential at control point p is defined as the weighted combination of the data cost of those pixels that have an impact on the control point p . The *unary* potential function is assumed to be independent of all other control points. Hence, it is approximated using two simplifications.²⁶ First, the elementary displacement of each image point \mathbf{x} (Eq. 1) is computed by a direct translation of d^p (the displacement of control point p), instead of resulting from the interpolation between the displacement of the neighboring control points. Second, with the aim to decrease the approximation error, the overlapping area for each control point is reduced by replacing the B-spline weighting functions in $\widehat{\eta}(\cdot)$ (Eq. 8) with linear ones. It should be reminded that B-spline functions are still kept to generate smooth transformation.

To have a full regularization, the deformation fields generated from the previous iterations are considered in the *pairwise* potential function as below:

$$V_{pq}(l_p, l_q) = |(\mathcal{R}(p) + d^p) - (\mathcal{R}(q) + d^q)|, \quad (10)$$

where $\mathcal{R}(\cdot)$ projects the current displacement fields on the level of the control points as:

$$\mathcal{R}(p) = \sum_{\mathbf{x} \in \Omega} \widehat{\eta}(|\mathbf{x} - p|) D(\mathbf{x}) \quad (11)$$

Various optimization strategies can be applied to find the registration parameters. An efficient algorithm

called FastPD is used in this study (for a full explanation of this method see Ref. 34). Some parameters controlling the discretization of the solution space have to be set. The first parameter is the maximum value of displacement which has been set to 0.4 times the current control point spacing.⁵⁵ To refine the deformation field, a multi-level FFD is employed to cover a wide range of transformations; for each level of control point spacing, a certain number of optimization cycles (the second parameter, O) is performed to model a large deformation. It should be noted that keeping the initial displacement set for each cycle does not bring any further improvement.²⁶ Therefore, each optimization cycle is done using a new set of displacement vectors. In this way, the initial maximum value of displacement is reduced by a scaling factor (the third parameter, α), and the new range is re-sampled using the same method (with a specific number of steps, the fourth parameter, n). For the results provided later, the parameters are set to $O = 5$, $\alpha = 0.67$ and $n = 5$.²⁶

Mesh Morphing

The atlas-to-subject volumetric image registration provides a pair of transformations that establishes a one-to-one correspondence between the two volumes (atlas J and subject I). The first one is a Rigid/Affine transformation ($T_{\text{Rigid/Affine}}$) that approximates the global transform between the two volumes, whereas the second one is a nonrigid transformation (T_{Nonrigid}) that locally refines the deformations. The next step towards atlas-mesh morphing consists in defining the total transformation by combining the rigid and non-rigid transformations:

$$T_{\text{Total}} = T_{\text{Nonrigid}} \circ T_{\text{Rigid/Affine}} \quad (12)$$

Depending on the type of atlas' FE mesh, various methods of mesh morphing could be employed to generate subject-specific FE meshes from the 3D displacement fields.^{4,5,12,15,35,57,68} In this paper our method will be used for linear FE meshes, in which nodes are connected by straight lines or edges. For this kind of mesh the mesh morphing procedure moves the nodes along the appropriate displacement fields (T_{Total}) while keeping the connectivities, preserving thus the topology of the atlas' mesh.

Evaluation

Image Registration Assessment

In order to quantitatively evaluate our method, manual segmentations of the atlas' and target's organs are used. After the registration between the atlas' and target's images, the obtained transformations are em-

ployed to deform the atlas' binary mask onto the target' images. Then, the Dice¹⁶ and volumetric overlap metrics, Hausdorff distance, and mean absolute surface are computed.²⁵ The Dice (**D**) and overlap fraction (**O**) are volumetric measures that compute the relative overlap of two volumes. For each subject, the Dice and volumetric overlap of the atlas-transformed mask ($V_{\text{Atlas-trans}}$) and the reference segmentation (V_{Manual}) are respectively defined as

$$\mathbf{D}(V_{\text{Atlas-trans}}, V_{\text{Manual}}) = \frac{2|V_{\text{Atlas-trans}} \cap V_{\text{Manual}}|}{|V_{\text{Atlas-trans}}| + |V_{\text{Manual}}|} \quad (13)$$

$$\mathbf{O}(V_{\text{Atlas-trans}}, V_{\text{Manual}}) = \frac{|V_{\text{Atlas-trans}} \cap V_{\text{Manual}}|}{|V_{\text{Atlas-trans}} \cup V_{\text{Manual}}|} \quad (14)$$

Both **D** and **O** values range from zero to one. A value close to one is desirable and means that there is a perfect match between the volumes. However, both volumetric measures depend on the size and shape complexity of the objects and on the volume sampling. Large objects such as the Lungs should be less sensitive to small local errors, which may exist at the boundaries. Therefore, the Hausdorff (**H**) distance is also considered as an evaluation of the similarity of the objects' surfaces. Given two surfaces $S_{\text{Atlas-trans}}$ and S_{Manual} , the Hausdorff distance is defined as

$$\mathbf{H}(S_{\text{Atlas-trans}}, S_{\text{Manual}}) = \max(h(S_{\text{Atlas-trans}}, S_{\text{Manual}}), h(S_{\text{Manual}}, S_{\text{Atlas-trans}})) \quad (15)$$

where

$$h(S_{\text{Atlas-trans}}, S_{\text{Manual}}) = \max_{p \in S_{\text{Atlas-trans}}} (d_{\min}(p, S_{\text{Manual}})), \quad (16)$$

$$h(S_{\text{Manual}}, S_{\text{Atlas-trans}}) = \max_{p \in S_{\text{Manual}}} (d_{\min}(p, S_{\text{Atlas-trans}})). \quad (17)$$

The Hausdorff distance is overly sensitive to outliers. A single outlier leads to misleading results. However, it can provide useful information in conjunction with other metrics such as the mean absolute surface distance (**M**), which is defined as

$$\mathbf{M}(S_{\text{Atlas-trans}}, S_{\text{Manual}}) = \frac{\bar{d}_{\min}(S_{\text{Atlas-trans}}, S_{\text{Manual}}) + \bar{d}_{\min}(S_{\text{Manual}}, S_{\text{Atlas-trans}})}{2} \quad (18)$$

where $\bar{d}_{\min}(S_{\text{Atlas-trans}}, S_{\text{Manual}})$ is the average minimum distance from all points on the surface $S_{\text{Atlas-trans}}$ to the

surface S_{Manual} , and vice-versa for $\bar{d}_{\min}(S_{\text{Manual}}, S_{\text{Atlas-trans}})$. \mathbf{M} indicates how much the two surfaces differ on average.

Mesh Quality Assessment

The regularity and quality of the deformed meshes are evaluated based on the Jacobian matrix.³³ The Jacobian matrix is the fundamental quantity describing all the *first – order* mesh properties (length, areas and angles) of interest.³³ The regularity assessment is a function of the Jacobian matrix determinant ($\det\mathbf{J}$, also called the *Jacobian*) and evaluates whether the employed FE mesh can be used for numerical analysis. The *Jacobian* must be checked for all the elements of the FE mesh as it is influenced by the configuration of the element nodes. Within each element, the *Jacobian* is computed for each node, and the element (and subsequently the FE mesh) is classified irregular if one of the nodes has a zero or negative value. It is worth pointing out that the *Jacobian* measures the distortion of the actual mesh element with respect to its reference configuration, but not the overall distortion information. To deal with this problem, the quality of each element can be determined at the level of its nodes (e.g., node n) by a ratio of nodal *Jacobian* value to the maximal *Jacobian* value among those computed at all element nodes (thus interpreted as a global distortion information). Such a ratio measures the node quality within its element (e) and is called Jacobian Ratio (\mathbf{JR}):³³

$$\mathbf{JR}_n^e = \frac{\det\mathbf{J}(n)}{\max_{n \in e} \{\det\mathbf{J}(n)\}} \quad (19)$$

The \mathbf{JR} values range from zero to one. Having a high (respectively low) value for \mathbf{JR}_n^e means that the element (e) has a high (respectively poor) quality at node n . The \mathbf{JR} is computed for all the element nodes and the minimum value is returned as an indicator of element quality (\mathbf{JR}_{\min}^e). In the ideal state, all elements of a given mesh are expected to have high \mathbf{JR} values; however in many cases this is impossible. That is why, for example, the commercial FE analysis software ANSYS sets a minimal value of $0.0\bar{3}$ for \mathbf{JR} .³¹ It should be noted that \mathbf{JR} is not relevant for tetrahedral elements as the *Jacobian* value is the same for all nodes of a tetrahedron which means that the \mathbf{JR} value is always one no matter how good or bad the element is. Therefore, we propose to measure the quality of tetrahedral elements by computing $\mathbf{Q} = 2\sqrt{6}R_{in}/L$ (R_{in} being the radius of the inscribed-sphere of the tetrahedron, and L the longest edge length^{18,21}). Similarly to \mathbf{JR} computed on hexahedra, wedges and pyramids, the \mathbf{Q} values computed on tetrahedra range from zero to one for low and high quality elements, respectively.

Finally, in order to complete the evaluation with quality criteria that can be computed on any type of element (hexahedra, tetrahedra, wedges and pyramids), we have used ANSYS software² to compute Aspect Ratio and Maximum Corner Angle for each element of the meshes.

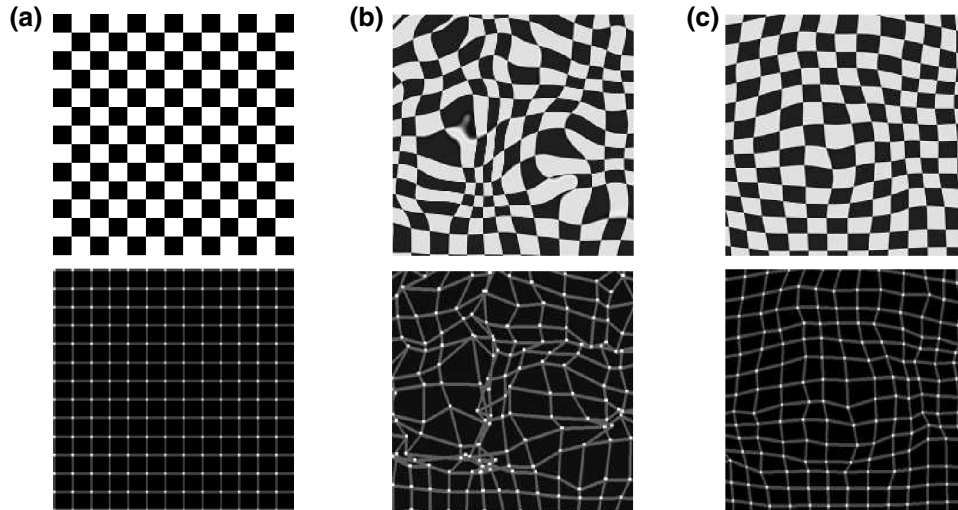
RESULTS

Before showing the results of mesh generation, it is important to illustrate how efficiently the regularization term prevents the introduction of foldings in the deformed meshes. Figure 4 shows the results of applying two transformations that are obtained without and with the regularization term. To have a clear understanding, only a section of the atlas' tongue mesh (including 11 elements) is selected and depicted. As can be seen, the level of mesh distortions is dramatically reduced by virtue of the regularization term. These two examples illustrate how the regularity and quality of the meshes can be preserved thanks to the diffeomorphic constraints and the regularization term. The value of the weight λ of the regularization term (Eq. 6) has to be set according to the application and to the measure of similarity. Generally, a higher λ value provides a smoother deformation thus less quality degradation, but sharp morphological structures are modeled less accurately. This raises the issue of the level of accuracy provided by our method. To address this issue we have applied our method to a data set of ribcage CT scans and compared the results with the manual segmentation of the Lungs also available in the data set.

Ribcage CT Image Registration

Subject-specific Lung's masks were generated with our method for 12 subjects. Since Lungs are large objects, the non-rigid registration was applied in two steps. First, the SAD similarity measure with a high value of λ (i.e., regularization weight) is employed in order to capture the main geometric properties of the target Lungs (with a very coarse initial control point spacing of 60 mm). Second, in order to get small details of the shape, the similarity measure is changed into SSD, and λ is decreased and an initial control point spacing of 25 mm is used. Figure 5 shows the result of the Lung registration for a typical CT scan. Manual Lungs segmentation in the atlas' image and in the target image are shown respectively in Fig. 5(a) and 5(b). The Lung's mask provided by our method is superimposed on the manual segmentation in Fig. 5(c). We observe a good agreement between both masks. However, the sharp regions, especially at the bottom of the Lungs, are captured less accurately. The Dice (\mathbf{D}),

Regularization effect at the level of image



Regularization effect at the level of mesh

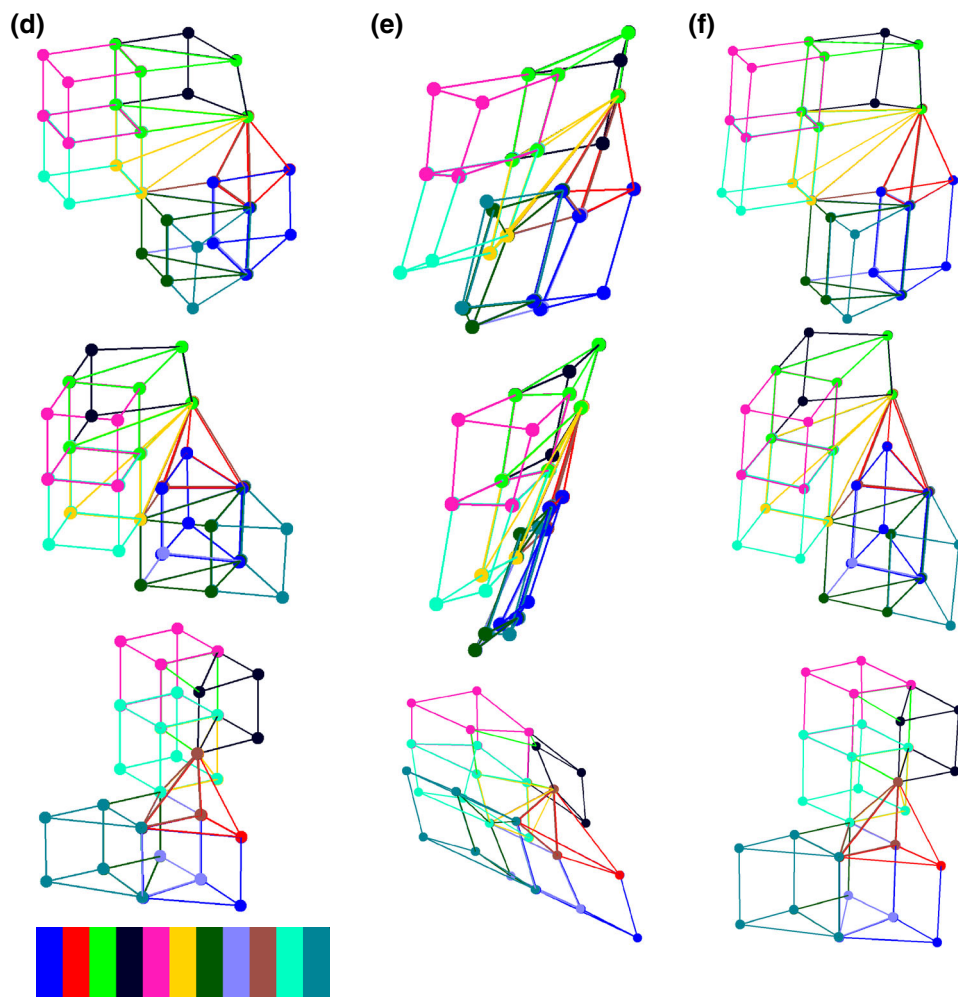


FIGURE 4. Effect of the regularization term: at the level of the image, (a) input image and the distribution of control points, (b) deformed input image without the regularization term and distribution of control points after registration, (c) deformed input image using the regularization term and distribution of control points after registration; and at the level of the mesh, (d) a section of the atlas FE Mesh, (e) deformed mesh without the regularization term (f) deformed mesh using the regularization term (different views are provided in each row: side, front, and back views, from top to bottom).



FIGURE 5. Result of the Lungs CT image registration: (a) Manual Lung segmentation in the atlas' CT-image (at each column, from left to right: front view, back view, and 3D ribcage CT reconstruction surrounding the Lung's manual segmentation), (b) Manual Lung's segmentation in a subject's CT-image (at each column, from left to right: front view, back view, and 3D ribcage CT reconstruction surrounding the Lung manual segmentation), (c) Atlas-driven subject-specific Lungs, in grey, superimposed on the manual segmentation, in red (at each column, from left to right: front view, back view, and a cut-out to the region having less accuracy).

overlap fraction (**O**), Hausdorff distance (**H**), and mean absolute surface (**M**) are calculated for all subjects. Means and standard deviations of these variables across the subjects are as follows: $\mathbf{D} = 0.98 \pm 0.01$, $\mathbf{O} = 0.96 \pm 0.01$, $\mathbf{H} = 34.25 \pm 7.75$ (in mm), and $\mathbf{M} = 0.98 \pm 0.26$ (in mm). The values of the average quality measures (**D**, **O**, and **M**) show that our method captures efficiently the geometry of target organs; however, high values of **H** are observed, which show the existence of some strong differences between both

masks at some places and/or for some subjects. This will be discussed later in this paper.

FE Tongue Meshes Generation

The subject-specific tongue FE meshes are shown in Fig. 6. The data set includes two healthy subjects and two patients suffering from tongue cancer. The regularity and quality of generated meshes are assessed

TABLE 1. Mesh quality distribution for the atlas' and subject's FE tongue meshes generated by our method; the regularities and qualities of the elements are quantified by computing JR (for pyramids, wedges, and hexahedra) and Q (for tetrahedra).

Meshes	# of irregular elements	Mesh quality (%)					
		<0.03	0.03–0.2	0.2–0.4	0.4–0.6	0.6–0.8	0.8–1
Atlas	0	0	24.28	2.08	13.30	15.32	45.32
S1	0	0	24.28	3.40	14.50	17.97	39.85
S2	0	0	24.28	3.15	14.00	15.26	43.31
P1	0	0	24.28	2.40	16.20	13.30	43.82
P2	0	0	24.28	5.80	12.86	18.63	38.43

TABLE 2. Mesh quality assessment for the atlas' and subject's FE tongue meshes generated by our method.

Meshes	Aspect ratio			Maximum corner angle		
	Warning count	Error count	Warn + Err (%)	Warning count	Error count	Warn + Err (%)
Atlas	0	0	0.00	0	0	0.00
S1	0	0	0.00	4	0	0.13
S2	2	0	0.06	2	0	0.06
P1	0	0	0.00	0	0	0.00
P2	2	0	0.06	2	0	0.06

Aspect Ratio: WARNING TOLERANCE = 20, and ERROR TOLERANCE = 1000000; Maximum Corner Angle: WARNING TOLERANCE = 165 (in degree), and ERROR TOLERANCE = 179.9 (in degree).

using the **JR** and **Q** (for tetrahedra). The results are presented in Table 1. None of the meshes contains any irregular element (**JR** < 0 or **Q** = 0). To have a more detailed assessment of mesh quality, the elements are classified into six categories. None of the meshes includes any element with a **JR** or **Q** smaller than the threshold 0.03 considered to characterize unacceptable poor quality. Also, the obtained values for Aspect Ratio and Maximum Corner Angle are reported in Table 2, indicating that all deformed meshes are regular. Our method is efficient to generate subject-specific FE meshes while preserving the regularity and quality of the elements.

Figure 7 focuses on the results obtained for subject S1. The external contours of the FE mesh are superimposed with sagittal, axial and coronal slices extracted from the MR exam. The enlarged tongue regions for some slices are provided in Fig. 7(d)–7(g). In addition, elements-size-distribution for the atlas FE tongue mesh and their nodal displacements, when our method is applied to S2 depending on whether the constraints are used or not, are shown in Fig. 8. The generated mesh using the pure non-rigid transformations contains 58 irregular elements. Volumes of all elements are computed and plotted in Fig. 8(a), according to their element-order within the original mesh file. Figure 8(b) displays the difference (in mm) between the maximal and the minimal nodal displacements for all element. This gives an interesting information since large differences are likely to be associated with strong geometrical distortions of the

elements. Figure 7 focuses on the results obtained for subject S1. The external contours of the FE mesh are superimposed with sagittal, axial and coronal slices extracted from the MR exam. The enlarged tongue regions for some slices are provided in Fig. 7(d)–7(g). In addition, elements-size-distribution for the atlas FE tongue mesh and their nodal displacements, when our method is applied to S2 depending on whether the constraints (i.e., the regularization term) are used or not, are shown in Fig. 8. The generated mesh using the pure (i.e., without the regularization term) non-rigid transformations contains 58 irregular elements. Volumes of all elements are computed and plotted in Fig. 8(a), according to their element-order within the original mesh file. Figure 8(b) displays the difference (in mm) between the maximal and the minimal nodal displacements for all elements. This gives an interesting information since large differences are likely to be associated with strong geometrical distortions of the element.

Qualitative Evaluation with a Patient-Specific Tongue Model

For patient P2, the activation of the posterior genio-glossus (GGp) muscle (one of the most important muscles of the tongue) is simulated before and after surgery. This muscle compresses the tongue in its lower part and its activation propels the tongue frontwards and upwards in its front part, as a consequence of the quasi-incompressibility of the tissues. Its role in speech

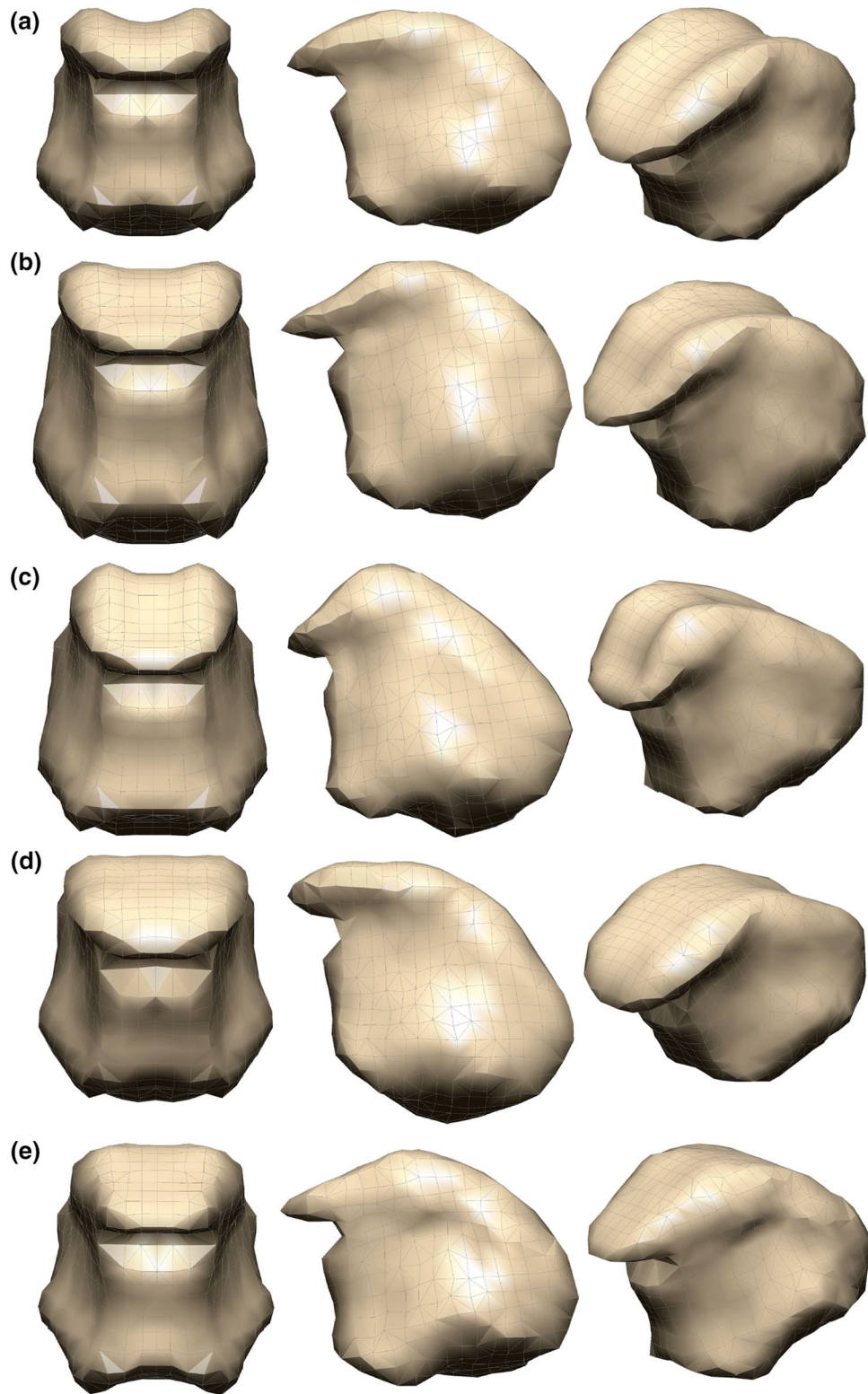


FIGURE 6. Result of atlas' FE mesh morphing using our method: (a) Atlas' FE tongue mesh (b) Subject-specific FE tongue mesh (subject S1), (c) subject-specific FE tongue mesh (subject S2), (d) Patient-specific FE tongue mesh (patient P1), (e) Patient-specific FE tongue mesh (patient P2).

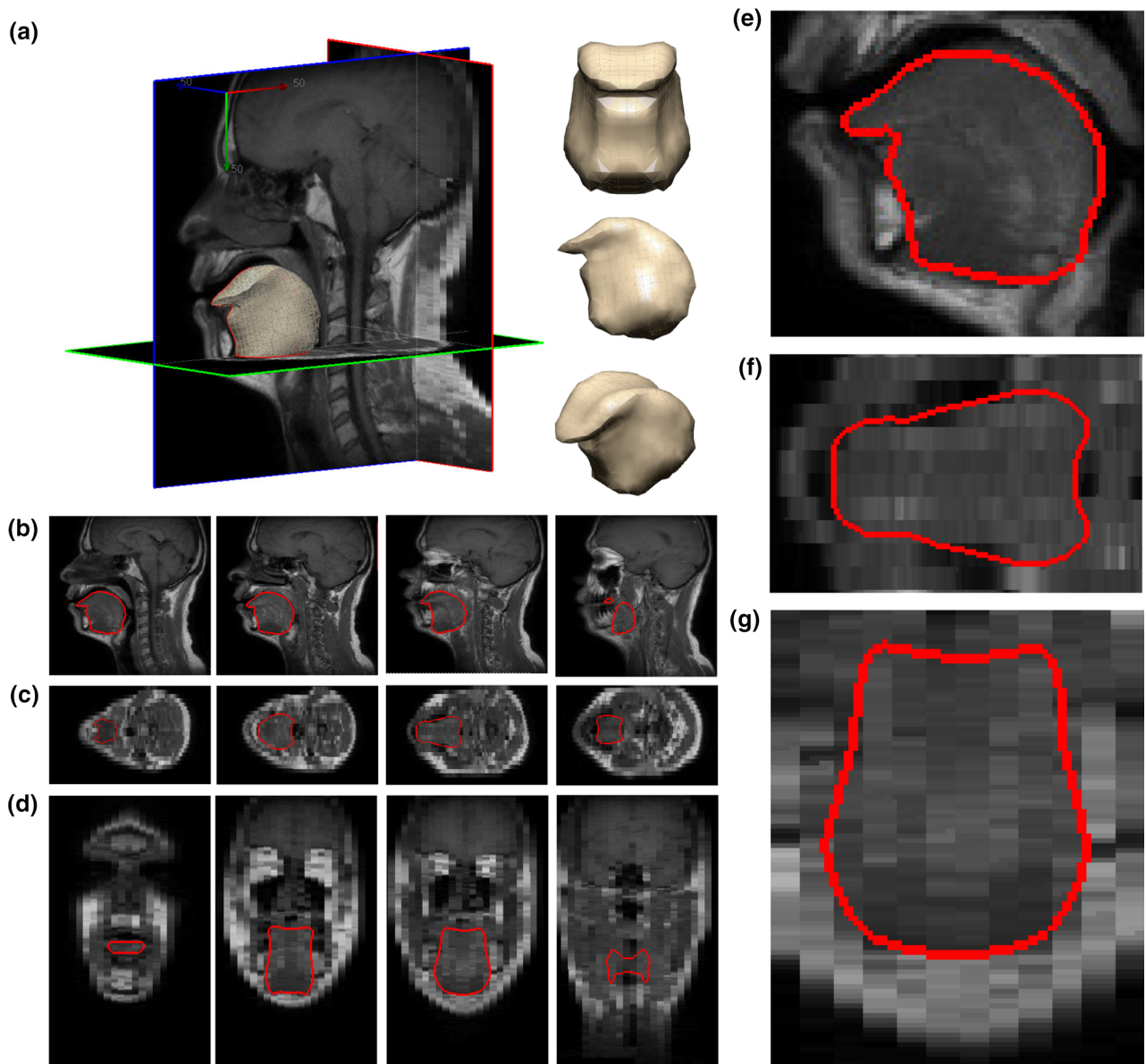


FIGURE 7. Mesh derived tongue contours superimposed on the MR image: (a) 3D subject-specific FE tongue mesh (Normal #1), (b) Sagittal views (mid-sagittal to the lateral side), (c) Axial views (inferior to superior), (d) Coronal views (anterior to posterior), (e) enlargement of the tongue region in a sagittal slice, (f) enlargement of the tongue region in the coronal slice, (g) enlargement of the tongue region in an axial slice.

production is crucial since it is strongly involved in the production of the phonemes /i/ and /s/, which exist in all the world languages. Muscle activation is modeled using the FE formulation of the Hill muscle model proposed by.^{8,50} This model was implemented using the USERMAT functionality of ANSYS. For the passive response, we used a simplified 5-parameter Mooney-Rivlin hyperelastic model with constitutive parameters ($C10 = 1037$ Pa, $C20 = 486$ Pa and bulk modulus $K = 2.107$ Pa) derived from previous work.¹¹ As concerns boundary, the nodes located in the front (which should be in contact with the mandible) and at

the bottom of the tongue are fixed (i.e., all 6 degrees of freedom are fixed $u1 = u2 = u3 = r1 = r2 = r3 = 0$). The assignment of the muscle fiber direction in each element in the tongue mesh is performed automatically based on the fibers direction extracted for the atlas' mesh in a previous work.²⁴ Tongue surgery consisted of a hemi-glossectomy during which half the upper tongue, mainly made of muscle tissues, has been removed and reconstructed with a flap having passive mechanical properties. It is accounted for in the tongue model by modifying the biomechanical properties of the excised tongue tissues: the active material proper-

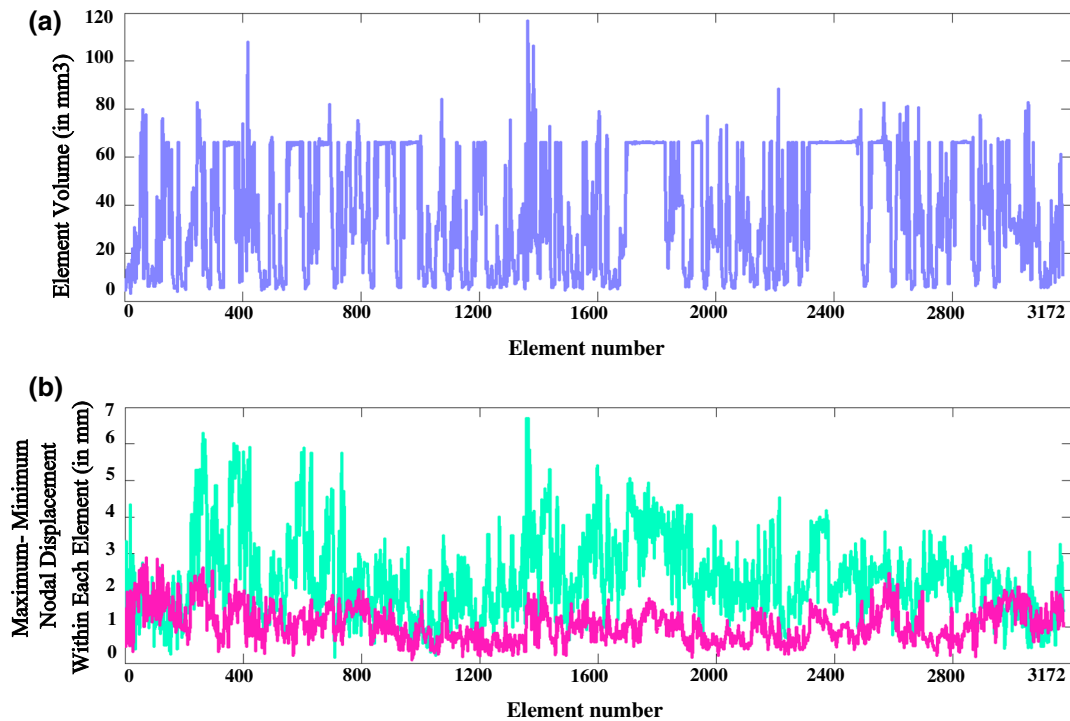


FIGURE 8. Representation of elements size in the atlas FE tongue mesh, and their displacements with and without constraints: (a) Elements-volumes-distribution for the atlas FE tongue mesh (in mm^3), (b) Maximum-Minimum nodal displacement (in mm) within each element for subject S2 in the mesh generated with the constraints (purple) and in the mesh generated without constraints (green), which contains 58 irregular elements ($JR < 0$ or $Q = 0$).

ties of the GGp elements that are removed and reconstructed are replaced with passive material properties.

Figure 9 plots the response of the tongue model to the activation of the GGp before and after the hemiglossectomy. Both the distribution of the Von mises equivalent strain in the GGp muscle and the displacement of the tongue are provided.

DISCUSSION

In this paper an original method for automatic subject-specific FE mesh generation is proposed and evaluated. Contrary to the previous efforts in the literature, our method does not require any formal extraction of prior-knowledge on the shape of the target organ, no meshing algorithm. We propose to use an image-based registration method to deform an atlas FE mesh and to automatically generate subject-specific meshes.

Our method was first evaluated on a publicly available set of images of the ribcage by comparing manual segmentations of the lungs for various subjects with the subject-specific Lungs masks obtained with

our method. Two steps were used, the first one with a parameterization adapted to the capture of global geometrical properties and the second one with a parameterization adapted to the capture of finer details. The match between results provided by both methods is very good in average as shown by the Dice, the overlap fraction and the mean average distance. However, the Hausdorff distance shows that strong differences might exist at some places. A careful analysis of our results shows that these strong differences occur in sharp regions that exist only in the atlas' or in the subject's images. This is a well-known problem in registration methods, as shown for example in Refs. 22,40,44,65. Applying a third registration step with less strong constraints might be useful. Another idea would be to use a third registration step that does not include any mesh quality preservation constraints. These possible solutions will be investigated in a future work, in particular to check whether the quality of the elements in the deformed meshed is still preserved. Also, multi-atlas approaches can partly overcome some of these errors by selection of the most similar atlas among a large database.¹ Figure 6 illustrates well the capacity of the method to generate various kinds of speaker-specific tongue anatomy at rest. From a more

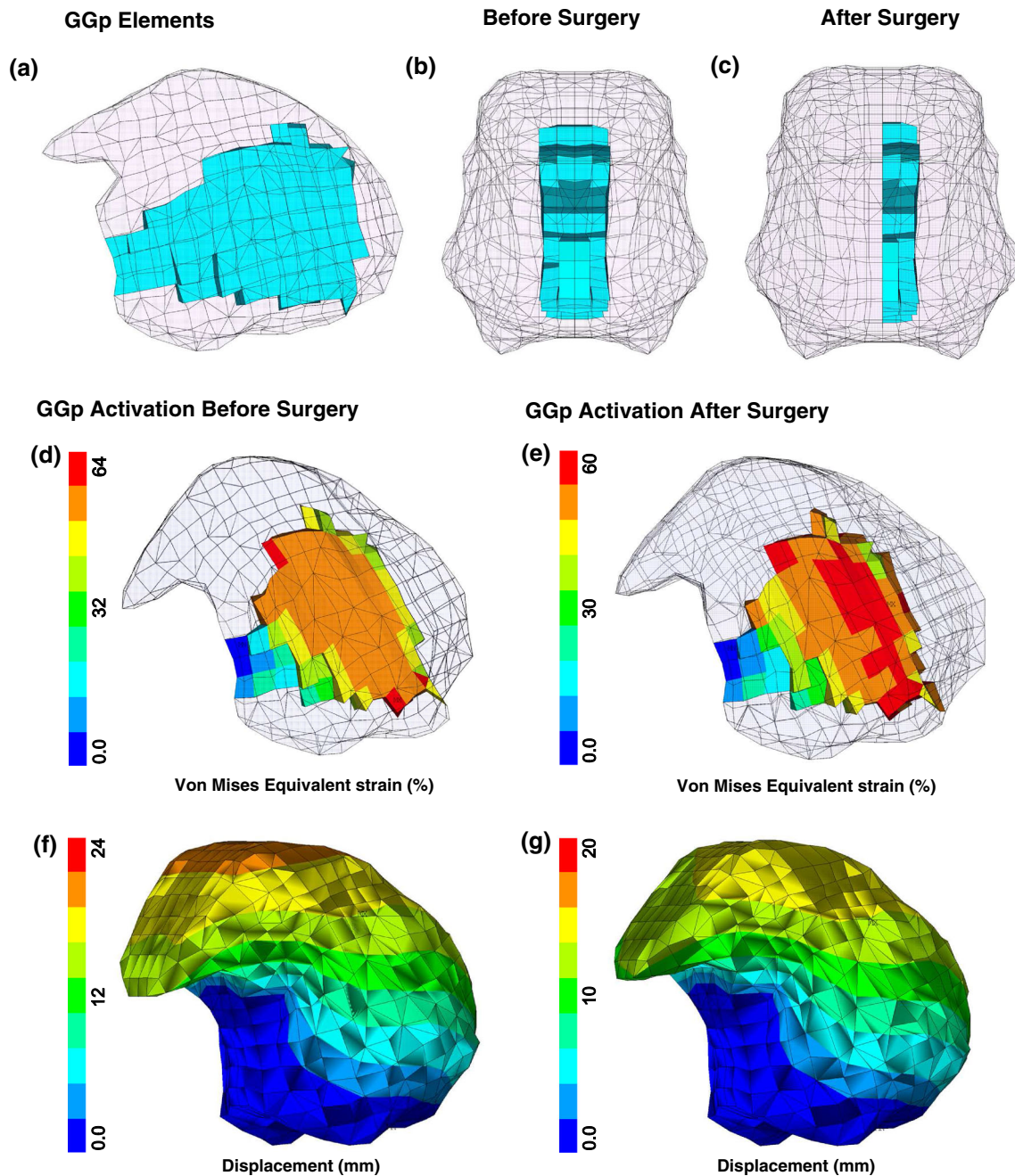


FIGURE 9. Biomechanical response of the tongue model to the activation of the GGp before and after surgery: (a) Sagittal view of the tongue showing the implementation of the GGp, (b) Front view of the tongue before surgery, (c) Front view of the tongue after surgery; the right part of the muscle has been removed and replaced by passive tissues, (d) Distribution of the Von Mises equivalent strain in the GGp after its activation in pre-surgery condition, (e) Distribution of the Von Mises equivalent strain in the GGp after its activation in post-surgery condition, (f) Displacement map in the tongue after GGP activation in pre-surgery condition, (g) Displacement map in the tongue after GGP activation in post-surgery condition.

quantitative point of view, the quality assessments reveal that the regularity and quality of the meshes are preserved. Contrary to Mesh-Morphing methods that sometimes need to post-process the mesh because of irregular elements,¹³ all generated meshes are regular

and can be used for FE analysis. Moreover, the quality of the mesh is almost maintained. Indeed, the percentage of elements within the quality range of 0.8–1 is slightly decreased by less than 7% (Table 1). This small reduction in the number of high quality elements re-

sults in small increment in the lower quality ranges (maximally 3.31, 2.9, and 3.72% for the ranges of 0.6–8, 0.4–0.6, and 0.2–0.4 respectively).

Figure 7 plots the contours of one generated mesh superimposed with the corresponding MR slices. The various slices displayed in the figure illustrate the efficiency of the method since the contours fit well with the observed boundaries of tongue tissues. Moreover, for some slices for which it is quite difficult to see tongue contours (the lateral sagittal views close to cheeks' tissues or tongue basement), registration method is able to suggest tongue contours thus maintaining a coherent structure for the whole 3D mesh. In Fig. 8 results of our method and the pure non-rigid registration are shown for S2. The maximal difference between the maximum and the minimum displacements within each element is decreased from 6.69 to 2.87 mm. This means that the probability of strong element distortion is significantly reduced and that the employed constraints have managed to control the movement of nodes within the elements.

Focusing on patient P2, we have proposed to simulate some functional consequences of a tongue surgery. Whereas the relevance of such use of a biomechanical model for computer assisted surgery has already been provided,¹⁰ the objective here was to propose an illustration of a tentative fully automatic procedure compatible with the clinical constraints. Therefore, starting from an MRI exam of a patient, we were able to automatically generate an FE model of that patient. All the information included in the tongue atlas model was automatically transferred in the model of the patient. It was thus straightforward to simulate the activation of the posterior genioglossus muscle. The corresponding results provided by Fig. 9 confirm a clinical observation, namely the fact that, after a hemiglossectomy, the tongue response is no longer symmetric. The results also predict that the patient might have difficulties to move the tongue in the front and upper part of the oral cavity since the simulated displacements after surgery are significantly lower than the ones simulated before hemiglossectomy.

The atlas-based subject-specific FE model generation method proposed in this paper seems to provide efficient results that were qualitatively and quantitatively evaluated on four subjects. Tongue models were used here since it is a clinical case for which the manual delineation of tongue contours is a particularly complex and sometimes impossible task.²⁸ The counterpart of this choice is that it is impossible to design a “gold standard” case to which we could compare the results proposed by our method. Indeed, since boundaries are difficult to identify for some regions of the tongue (e.g., at the bottom and laterally), we were not able to ask an “expert” to segment a whole tongue and to guaranty

that this segmentation would be considered as the “gold standard”. In any case it seems clear that when the disease is advanced and the size of tumors are high, the general shape of the target organ is divided into sub-shapes. In other words, the tumors can be considered as new organs inside the target organ that disturb the registration process. To sum up, when the original shape is still remained or there is no significant tumor size progression, the proposed method, that employs a multi-level FFDs, is able to capture the geometry of the organs well.

Our method still needs to define the weighting factor lambda that controls the influence of the regularization term. This highly depends on the image modality as well as the type of organ. Our method needs therefore definitively to be more extensively evaluated on a larger set of tongue MR images.

ACKNOWLEDGMENTS

This work was partly funded by the AGIR program (Grenoble Universities) and by the ANR under reference ANR-11-LABX-0004. We are grateful to Georges Bettega (Grenoble Hospital), Mayra Moya Espinosa (Ensam Paris), Chenchen Tong (National University of Singapore) and Marek Bucki (Taxisense Company) for many interactions and inputs to this study.

REFERENCES

- ¹Acosta, O., A. Simon, F. Monge, *et al.* Evaluation of multi-atlas-based segmentation of CT scans in prostate cancer radiotherapy. In: IEEE International Symposium on Biomedical Imaging: From Nano to Macro, pp. 1966–1969, 2011.
- ²ANSYS Inc, ANSYS Fluent, 2015. Available from: www.ansys.com.
- ³Badin, P., P. Borel, G. Bailly, L. Revret, M. Baciuc, and C. Segebarth. Towards an audiovisual virtual talking head: 3D articulatory modeling of tongue, lips and face based on MRI and video images. In: 5th Speech Production Seminar, 2000 pp. 261–264.
- ⁴Bah, M. T., P. B. Nair, and M. Browne. Mesh morphing for finite element analysis of implant positioning in cementless total hip replacements. *Medical engineering and physics*, 31(10): 1235–1243, 2009.
- ⁵Baldwin, M. A., J. E. Langenderfer, P. J. Rullkoetter, and P. J. Laz. Development of subject-specific and statistical shape models of the knee using an efficient segmentation and mesh-morphing approach. *Computer methods and programs in biomedicine*. 97(3): 232–240, 2010.
- ⁶Barber, D. C., E. Oubel, A. F. Frangi, and D. R. Hose. Efficient computational fluid dynamics mesh generation by image registration. *Medical image analysis*. 11(6): 648–662, 2007.

- ⁷Benzley, S. E., E. Perry, K. Merkle, B. Clark, and G. Sjaardama. A comparison of all hexagonal and all tetrahedral finite element meshes for elastic and elastoplastic analysis. In: Proceedings of the 4th International Meshing Roundtable, vol. 17 pp. 179–191, 1995.
- ⁸Blemker, S. S., P. M. Pinsky, and S. L. Delp. A 3D model of muscle reveals the causes of nonuniform strains in the biceps brachii. *Journal of biomechanics*. 38(4): 657–665, 2005.
- ⁹Breiman, L., J. Friedman, C. J. Stone, and R. A. Olshen. *Classification and Regression Trees*. Boca Raton: CRC Press, 1984.
- ¹⁰Buchaillard, S., M. Brix, P. Perrier, and Y. Payan. Simulations of the consequences of tongue surgery on tongue mobility: implications for speech production in post-surgery conditions. *The International Journal of Medical Robotics and Computer Assisted Surgery*. 3(3), 252–261, 2007.
- ¹¹Buchaillard, S., P. Perrier, and Y. Payan. A biomechanical model of cardinal vowel production: Muscle activations and the impact of gravity on tongue positioning. *The Journal of the Acoustical Society of America*. 126(4): 2033–2051, 2009.
- ¹²Bucki, M., C. Lobos, and Y. Payan. A fast and robust patient specific finite element mesh registration technique: application to 60 clinical cases. *Medical image analysis*. 14(3): 303–317, 2010.
- ¹³Bucki, M., C. Lobos, Y. Payan, and N. Hitschfeld. Jacobian-based repair method for finite element meshes after registration. *Engineering with Computers*. 27(3): 285–297, 2011.
- ¹⁴Chenchen, T. *Generation of Patient-Specific Finite-Element Mesh from 3D Medical Images*. Doctoral dissertation, National University of Singapore, 2013.
- ¹⁵Couteau, B., Y. Payan, and S. Lavallée. The mesh-matching algorithm: an automatic 3D mesh generator for finite element structures. *Journal of biomechanics*. 33(8): 1005–1009, 2000.
- ¹⁶Dice, L. R. Measures of the amount of ecologic association between species. *Ecology*, 26.3: 297–302, 1945.
- ¹⁷Dittrich, T. G. Machine learning research: four current directions. *Artificial Intelligence Magazine*. 4: 97–136, 1997.
- ¹⁸Du, Q., and D. Wang. The optimal centroidal Voronoi tessellations and the gershon's conjecture in the three-dimensional space. *Computers and Mathematics with Applications*. 49.9, 1355–1373, 2005.
- ¹⁹Fang, Q., and D. A. Boas. Tetrahedral mesh generation from volumetric binary and gray-scale images. In: *ISBI'09 Proceedings of the 6th IEEE International Conference on Symposium on Biomedical Imaging: From Nano to Macro*, Boston, MA, pp. 1142–1145, 2009.
- ²⁰Fernandez, J. W., P. Mithraratne, S. F. Thrupp, M. H. Tawhai, and P. J. Hunter. Anatomically based geometric modelling of the musculo-skeletal system and other organs. *Biomechanics and modeling in mechanobiology*. 2(3): 139–155, 2004.
- ²¹Field, D. A. Qualitative measures for initial meshes. *International Journal for Numerical Methods in Engineering*. 47.4, 887–906, 2000.
- ²²Garcia, V., O. Commowick, and G. Malandain. A robust and efficient block matching framework for non linear registration of thoracic CT images. In: *Grand Challenges in Medical Image Analysis (MICCAI workshop)*, 2010, pp. 1–10.
- ²³Geman, S., and D. Geman. Stochastic relaxation, Gibbs distributions, and the Bayesian restoration of images. *IEEE Transactions on Pattern Analysis and Machine Intelligence*. 6: 721–741, 1984.
- ²⁴Gerard, J.M., R. Wilhelms-Tricarico, P. Perrier, and Y. Payan. A 3D dynamical biomechanical tongue model to study speech motor control. *Recent Research Developments in Biomechanics*. 1: 49–64, 2003.
- ²⁵Gerig, G., M. Jomier, and M. Chakos. A new validation tool for assessing and improving 3D object segmentation. In *Lecture Notes in Computer Science*. Berlin, Germany: Springer, pp. 516–523, 2001.
- ²⁶Glocker, B., N. Komodakis, G. Tziritas, N. Navab, and N. Paragios. Dense image registration through MRFs and efficient linear programming. *Medical image analysis*. 12(6): 731–741, 2008.
- ²⁷Grassi, L., N. Hraiech, E. Schileo, M. Ansaloni, M. Rochette, and M. Viceconti. Evaluation of the generality and accuracy of a new mesh morphing procedure for the human femur. *Medical engineering and physics*. 33(1): 112–120, 2011.
- ²⁸Harandi, M. N., R. Abugharbieh, and S. Fels. 3D segmentation of the tongue in MRI: a minimally interactive model-based approach. *Computer Methods in Biomechanics and Biomedical Engineering: Imaging & Visualization*. 2014. doi:10.1080/21681163.2013.864958.
- ²⁹Iskarous, K. Patterns of tongue movement. *Journal of Phonetics*, 33(4), 363–381, 2005.
- ³⁰Ji, S., J. C. Ford, R. M. Greenwald, J. G. Beckwith, K. D. Paulsen, L. A. Flashman, and T. W. McAllister. Automated subject-specific, hexahedral mesh generation via image registration. *Finite Elements in Analysis and Design*. 47(10): 1178–1185, 2011.
- ³¹Kelly S. Element shape testing. In: *Ansys Theory Reference*, Chap 13, Ansys, USA, 1998.
- ³²Keyak, J. H., J. M. Meagher, H. B. Skinner, and C. D. Mote. Automated three-dimensional finite element modeling of bone: A new method. *Journal of Biomedical Engineering*. 12(5): 389–397, 1990.
- ³³Knupp, P. M. Achieving finite element mesh quality via optimization of the Jacobian matrix norm and associated quantities. Part II—a framework for volume mesh optimization and the condition number of the Jacobian matrix. *International Journal for numerical methods in engineering*. 48(8): 1165–1185, 2000.
- ³⁴Komodakis, N., G. Tziritas, and N. Paragios. Fast, approximately optimal solutions for single and dynamic MRFs. In: *IEEE Conference on Computer Vision and Pattern Recognition (CVPR'07)*, pp. 1–8, 2007.
- ³⁵Lamata, P., S. Niederer, D. Nordsletten, D. C. Barber, I. Roy, D. R. Hose, and N. Smith. An accurate, fast and robust method to generate patient-specific cubic Hermite meshes. *Medical image analysis*. 15(6): 801–813, 2011.
- ³⁶Lamata, P., I. Roy, B. Blazevic, A. Crozier, S. Land, S. A. Niederer, D. Hose, and N. P. Smith. Quality metrics for high order meshes: analysis of the mechanical simulation of the heart beat. *IEEE Transactions on Medical Imaging*, 32(1): 130–138, 2013.
- ³⁷Lederman, C., A. Joshi, I. Dinov, L. Vese, A. Toga, and J. D. Van Horn. The generation of tetrahedral mesh models for neuroanatomical MRI, *NeuroImage*. 55(1): 153–164, 2011.
- ³⁸Lee, J., J. Woo, F. Xing, E. Z. Murano, M. Stone, and J. L. Prince. Semi-automatic segmentation for 3D motion anal-

- ysis of the tongue with dynamic MRI. *Computerized Medical Imaging and Graphics*. 38(8): 714–724, 2014.
- ³⁹Li, S. Z. Markov random field modeling in image analysis. Springer Science Business Media, 2009.
- ⁴⁰Li, B., G. E. Christensen, J. Dill, E. A. Hoffman, and J. M. Reinhardt. 3D intersubject warping and registration of pulmonary CT images for a human lung model. In *Medical Imaging, International Society for Optics and Photonics*, pp. 324–335, 2002.
- ⁴¹Lobos, C. A set of mixed-elements patterns for domain boundary approximation in hexahedral meshes. In *MMVR*, pp. 268–272, 2013.
- ⁴²Lobos, C., Y. Payan, and N. Hitschfeld. Techniques for the generation of 3D Finite Element Meshes of human organs. In A. Daskalaki (Ed.), *Informatics in Oral Medicine: Advanced Techniques in Clinical and Diagnostic Technologies*. Hershey, PA: Medical Information Science Reference. 126–158, 2010.
- ⁴³Maes, F., A. Collignon, D. Vandermeulen, G. Marchal, and P. Suetens. Multimodality image registration by maximization of mutual information. *IEEE Transactions on Medical Imaging*. 16(2): 187–198, 1997.
- ⁴⁴Mansoor, A., U. BAGCI, B. FOSTER, *et al.* Segmentation and Image Analysis of Abnormal Lungs at CT: Current Approaches, Challenges, and Future Trends. *RadioGraphics*. 35(4), 1056–1076, 2015.
- ⁴⁵Mattes, D., D. R. Haynor, H. Vesselle, T. K. Lewellen, and W. Eubank. PET-CT image registration in the chest using free-form deformations. *IEEE Transactions on Medical Imaging*. 22(1), 120–128, 2003.
- ⁴⁶Mitchell, S. A., A Technical History of Hexahedral Mesh Generation. In: 11th International Meshing Roundtable, short course, 2002.
- ⁴⁷Mohamed, A., and C. Davatzikos. Finite element mesh generation and remeshing from segmented medical images. In: *ISBI'04 Proceedings of the 6th IEEE International Conference on Symposium on Biomedical Imaging: From Nano to Macro*, vol. 1, pp. 420–423, 2004.
- ⁴⁸Molino, N., R. Bridson, J. Teran, and R. Fedkiw. A Crystalline, Red Green Strategy for Meshing Highly Deformable Objects with Tetrahedra. In: 12th International Meshing Roundtable, Santa Fe, New Mexico, USA. 103–114, 2003.
- ⁴⁹Murphy, K., B. Van Ginneken, J. M. Reinhardt, S. Kabus, K. Ding, X. Deng, K. Cao *et al.* Evaluation of registration methods on thoracic CT: the EMPIRE10 challenge. *Medical Imaging, IEEE Transactions on* 30, no. 11: 1901–1920, 2011.
- ⁵⁰Nazari, M. A., P. Perrier, and Y. Payan. The Distributed Lambda (λ) Model (DLM): a 3D, Finite-element muscle model based on feldman's λ model assessment of orofacial gestures. *Journal of speech, language, and hearing research*. 56(6): 1909–1923, 2013.
- ⁵¹Nikos, K., G. Tziritas, and N. Paragios. Performance vs computational efficiency for optimizing single and dynamic MRFs: Setting the state of the art with primal-dual strategies. *Computer Vision and Image Understanding*. 112(1): 14–29, 2008.
- ⁵²Powell, M.J.D. A fast algorithm for nonlinearly constrained optimization calculations. In: *Numerical Analysis*, Berlin: Springer, pp. 144–157, 1987.
- ⁵³Roche, A., G. Malandain, X. Pennec, and N. Ayache. The correlation ratio as a new similarity measure for multimodal image registration. In: *Medical Image Computing and Computer-Assisted Intervention-MICCAI*, Springer, Berlin, pp. 1115–1124, 1998.
- ⁵⁴Rohan, P-Y., C. Lobos, M. A. Nazari, P. Perrier, and Y. Payan. Finite element modelling of nearly incompressible materials and volumetric locking: a case study. *Computer methods in biomechanics and biomedical engineering*. 17(sup1), 192–193, 2014.
- ⁵⁵Rueckert, D., P. Aljabar, R. A. Heckemann, J. V. Hajnal, and A. Hammers. Diffeomorphic registration using B-splines. In: *Medical Image Computing and Computer-Assisted Intervention “MICCAI*, Berlin: Springer, pp. 702–709, 2006.
- ⁵⁶Rueckert, D., L. I. Sonoda, C. Hayes, D. LG Hill, M. O. Leach, and D. J. Hawkes. Non-rigid registration using free-form deformations: Application to breast MR images, *IEEE Transactions on Image Processing*. 18(8): 712–721, 1999.
- ⁵⁷Sigal, I. A., M. R. Hardisty, and C. M. Whyne. Mesh-morphing algorithms for specimen-specific finite element modeling. *Journal of biomechanics*, 41(7): 1381–1389, 2008.
- ⁵⁸Tautges, T. J., T. Blacker, and S. A. Mitchell. The whisker weaving algorithm: A connectivity-based method for constructing all-hexahedral finite element meshes. *International Journal for Numerical Methods in Engineering*. 39.19: 3327–3349, 1996.
- ⁵⁹Van Rikxoort, E. M., B. D. Hoop, M. A. Viergever, M. Prokop, and B. V. Ginneken. Automatic lung segmentation from thoracic computed tomography scans using a hybrid approach with error detection. *Medical physics* 36, no. 7: 2934–2947, 2009.
- ⁶⁰Vercauteren, T., X. Pennec, A. Perchant, and N. Ayache. Diffeomorphic demons: Efficient non-parametric image registration. *NeuroImage*. 45(1): S61–S72, 2009.
- ⁶¹Viceconti, M., and F. Taddei. Automatic generation of finite element meshes from computed tomography data. *Critical Reviews™ in Biomedical Engineering*. 31(1-2): 27–72, 2003.
- ⁶²Viceconti, M., M. Davinelli, F. Taddei, and A. Cappello. Automatic generation of accurate subject-specific bone finite element models to be used in clinical studies, *Journal of Biomechanics*. 37:1597–1605, 2004.
- ⁶³Weatherill, N. P., and O. Hassan. Efficient three-dimensional Delaunay triangulation with automatic point creation and imposed boundary constraints. *International Journal for Numerical Methods in Engineering*. 12: 2005–2039, 1994.
- ⁶⁴Wright, S. J., and J. Nocedal. *Numerical optimization*. Vol. 2. New York: Springer, 1999.
- ⁶⁵Zhang, L., and J. M. Reinhardt. 3D pulmonary CT image registration with a standard lung atlas. In: *Medical Imaging, International Society for Optics and Photonics*, pp. 67–77, 2000.
- ⁶⁶Zhang, Y., C. Bajaj, and B. S. Sohn. 3D finite element meshing from imaging data, *Computer Methods in Applied Mechanics and Engineering*. 194(48): 5083–5106, 2005.
- ⁶⁷Zhang, Y., T. JR. Hughes, and C. L. Bajaj. Automatic 3D mesh generation for a domain with multiple materials. In: *Proceedings of the 16th International Meshing Roundtable*, Springer, Berlin Heidelberg, pp. 367–386, 2008.
- ⁶⁸Zhang, S., Y. Zhan, X. Cui, M. Gao, J. Huang, and D. Metaxas. 3D anatomical shape atlas construction using mesh quality preserved deformable models. *Computer Vision and Image Understanding*, 117(9): 1061–1071, 2013.